





RESEARCH ARTICLE | SEPTEMBER 18 2024

Thermodynamic quantum Fokker–Planck equations and their application to thermostatic Stirling engine **FREE**

Special Collection: [Algorithms and Software for Open Quantum System Dynamics](#)


Shoki Koyanagi   ; Yoshitaka Tanimura  


 Check for updates


J. Chem. Phys. 161, 112501 (2024)


<https://doi.org/10.1063/5.0225607>




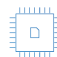
 Nanotechnology & Materials Science

 Optics & Photonics

 Impedance Analysis

 Scanning Probe Microscopy

 Sensors

 Failure Analysis & Semiconductors

Thermodynamic quantum Fokker–Planck equations and their application to thermostatic Stirling engine

Cite as: J. Chem. Phys. 161, 112501 (2024); doi: 10.1063/5.0225607

Submitted: 25 June 2024 • Accepted: 9 August 2024 •

Published Online: 18 September 2024



View Online



Export Citation



CrossMark

Shoki Koyanagi^{a)}  and Yoshitaka Tanimura^{a)} 

AFFILIATIONS

Department of Chemistry, Graduate School of Science, Kyoto University, Kyoto 606-8502, Japan

Note: This paper is part of the JCP Special Topic on Algorithms and Software for Open Quantum System Dynamics.

^{a)} **Authors to whom correspondence should be addressed:** koyanagi.syoki.36z@st.kyoto-u.jp
and tanimura.yoshitaka.5w@kyoto-u.jp

ABSTRACT

We developed a computer code for the thermodynamic quantum Fokker–Planck equations (T-QFPE), derived from a thermodynamic system–bath model. This model consists of an anharmonic subsystem coupled to multiple Ohmic baths at different temperatures, which are connected to or disconnected from the subsystem as a function of time. The code numerically integrates the T-QFPE and their classical expression to simulate isothermal, isentropic, thermostatic, and entropic processes in both quantum and classical cases. The accuracy of the results was verified by comparing the analytical solutions of the Brownian oscillator. In addition, we illustrated a breakdown of the Markovian Lindblad–master equation in the pure quantum regime. As a demonstration, we simulated a thermostatic Stirling engine employed to develop non-equilibrium thermodynamics [S. Koyanagi and Y. Tanimura, J. Chem. Phys. **161**, 114113 (2024)] under quasi-static conditions. The quasi-static thermodynamic potentials, described as intensive and extensive variables, were depicted as work diagrams. In the classical case, the work done by the external field is independent of the system–bath coupling strength. In contrast, in the quantum case, the work decreases as the coupling strength increases due to quantum entanglement between the subsystem and bath. The codes were developed for multicore processors using Open Multi-Processing (OpenMP) and for graphics processing units using the Compute Unified Device Architecture. These codes are provided in the [supplementary material](#).

Published under an exclusive license by AIP Publishing. <https://doi.org/10.1063/5.0225607>

I. INTRODUCTION

In contrast to classical thermodynamics, which is a macroscopic qualitative theory, quantum thermodynamics, described by the Hamiltonian, allows for dynamic investigations in addition to equilibrium cases. A commonly used model for describing thermodynamics is a system–bath (SB) model, which consists of a subsystem interacting with a harmonic heat bath.^{1–3} Due to quantum entanglement between the system and the bath (bathentanglement),⁴ the quantum SB system exhibits unique properties compared to the classical one, particularly at low temperatures. These include the negativity of the noise correlation function³ and deviations from the canonical equilibrium state.^{1–4} To simulate SB entanglement dynamics even under external driving forces, it is necessary to consider both energy relaxation and excitation from

the bath, which is related by the fluctuation–dissipation theorem,⁵ such as for the reduced density operator based-approaches as the hierarchical equations of motion (HEOM) approach,^{3–19} and the quasi-adiabatic path integral (QUAPI) approach.^{20–26} Note that the detailed balance and positivity conditions often assumed for the reduced description of the density operator are sufficient conditions resulting from an accurate description of the dynamics, but they are not necessary conditions. In quantum thermodynamics, which deals with the delicate energy balance between the subsystem and the bath, arguments based solely on sufficient conditions may lead to artifacts, such as breaking the second law of thermodynamics, by ignoring bathentanglement.

Among these, the HEOM are stable as long as a sufficient number of hierarchy elements are included and reliable, as their numerical accuracy has been confirmed through comparisons with

analytical solutions.⁹ This approach is suitable for thermodynamic investigations because it allows for numerically rigorous dynamic simulations and evaluates the SB interaction and bath parts of the energy, which cannot be assessed using the conventional reduced equation of motion approach, even for processes far from equilibrium.^{27–34}

It should be noted that there are two types of non-Markovian effects: one originating from the noise correlation time determined by the bath spectral distribution function (SDF) and the other from the bath temperature determined by the Matsubara frequency. The former is important for ultrafast vibrational, electronic, and excitonic processes in the condensed phase, where the subsystem's characteristic time scale and the environment's noise correlation time are both in the femtosecond to picosecond range. However, this is not essential in thermodynamic studies where the subsystem changes on the nanosecond scale or less. In contrast, the latter produces effects unique to quantum thermodynamics, such as changing the equilibrium distribution from a canonical one due to bathentanglement, even in the case of the Ohmic SDF without a cutoff.¹⁴

Thus, the low-temperature quantum Fokker–Planck equations (LT-QFPE)¹⁴ were derived from the Brownian (or Ullersma–Caldeira–Leggett) model^{35–37} for the Ohmic SDF, include the low-temperature Matsubara terms in the hierarchical form without resorting to the rotating wave and factorized approximations. The LT-QFPE are useful for thermodynamic exploration because they reduce the numerical simulation cost compared to the regular HEOM for the Drude SDF^{9–13} and makes it possible to take the classical limit to obtain the Kramers equation, which is equivalent to the Langevin equation used for thermodynamic simulations in molecular dynamics (MD) approaches. The source code of the LT-QFPE for simulating single and multi-state Brownian systems is presented as a supporting material in Ref. 14, along with a demo program comparing LT-QFPE results for non-adiabatic dynamic simulations with those of the fewest-switch surface hopping and Ehrenfest methods with a classical Markovian Langevin force. The results reveal the importance of the quantum low-temperature correction terms.

To construct a systematic theory of thermodynamics, it is essential to include a thermostatic process.³³ By introducing multiple baths at different temperatures, we can study a thermostatic process in which temperature varies with time. Assuming that the time scale of quantum thermal fluctuations is shorter than the time scale of the external perturbations, we can extend LT-QFPE to the thermostatic case by introducing time-dependent Matsubara frequencies, described as thermodynamic quantum Fokker–Planck equations (T-QFPE).^{33,34} This article presents an overview of the T-QFPE, provides the C++ source code for numerical simulations, and briefly explains its theoretical background to further the development of quantum thermodynamics.

In Sec. II, after explaining the thermodynamic SB Hamiltonian, we present the T-QFPE in the Wigner representation. In Sec. III, we verify the accuracy of the T-QFPE code by comparing it with analytical solutions of the Brownian oscillator. In Sec. IV, we then demonstrate the capability of our code by simulating the quasi-static processes of the thermostatic Stirling engine, presenting the work diagram in terms of intensive and extensive variables. Section V presents concluding remarks.

II. THERMODYNAMIC QUANTUM FOKKER–PLANCK EQUATIONS (T-QFPE)

The T-QFPE were developed for Ohmic SDF to investigate various thermodynamic processes, including isothermal, thermostatic, isentropic, thermostatic, and entropic processes.^{33,34} For these processes, the free energy can also be evaluated as a function of thermodynamic intensive and extensive variables by assessing the work done for changes in temperature and external fields. The model Hamiltonian of the T-QFPE is expressed as follows:

$$\hat{H}_{tot}(t) = \hat{H}_A(t) + \sum_{k=1}^N \hat{H}_{IB}^k(t), \quad (1)$$

where $\hat{H}_A(t)$ is the subsystem Hamiltonian. Here, we consider the case where the subsystem is described in phase space as

$$\hat{H}_A(t) = \frac{\hat{p}^2}{2m} + U(\hat{q}, t), \quad (2)$$

where \hat{q}, \hat{p}, m are the position operator, momentum operator, and particle mass, respectively, and $U(\hat{q}, t)$ is the potential. To treat thermostatic processes, in Eq. (1), we consider N heat baths with different temperatures T_k . The k th bath Hamiltonian including the system–bath (SB) interaction between the subsystem and the k th bath $\hat{H}_{IB}^k(t)$ is expressed as

$$\hat{H}_{IB}^k(t) = \sum_j \left\{ \frac{(\hat{p}_j^k)^2}{2m_j^k} + \frac{m_j^k (\omega_j^k)^2}{2} \left[\hat{x}_j^k - \frac{A_k \xi_k(t) c_j^k \hat{q}}{m_j^k (\omega_j^k)^2} \right]^2 \right\}, \quad (3)$$

where $\hat{x}_j^k, \hat{p}_j^k, m_j^k, \omega_j^k$, and c_j^k are the position operator, momentum operator, mass, angular frequency, and coupling coefficient of the j th mode in the k th bath, respectively, and A_k is the SB coupling strength between the subsystem and the k th bath. Here, $\xi_k(t)$ is the window function that is 1 when the bath is attached to the subsystem and 0 when it is not.

For the k th bath, the subsystem A is driven by the external force $\hat{X}^k(t)$ through the interaction $-V(\hat{q})\hat{X}^k$, where $\hat{X}^k(t)$ is the Heisenberg representation of $\hat{X}^k \equiv \sum_j c_j^k \hat{x}_j^k$ for \hat{H}_B^k . The character of the bath is determined by SDF of the k th bath, defined as $J_k(\omega) = \sum_j (A_k^2 (c_j^k)^2 / 2m_j^k \omega_j^k) \delta(\omega - \omega_j^k)$. Each bath being harmonic and Gaussian in nature, the character of $\hat{X}^k(t)$ is specified by its two-time correlation functions, such as the symmetrized and canonical correlation functions defined by $C^k(t) \equiv \langle \hat{X}^k(t) \hat{X}^k(0) + \hat{X}^k(0) \hat{X}^k(t) \rangle_B / 2$ and $R^k(t) \equiv \int_0^{\beta \hbar} d\lambda \langle \hat{X}^k(-i\hbar\lambda) \hat{X}^k(t) \rangle_B / 2$, where $\langle \cdots \rangle_B$ represents the thermal average of the k th bath degree of freedom.^{3,9}

The SDF of the k th bath is defined as $J_k(\omega) = \sum_j (A_k^2 (c_j^k)^2 / 2m_j^k \omega_j^k) \delta(\omega - \omega_j^k)$, and we assume that it is the Ohmic SDF expressed as

$$J_k(\omega) = \frac{A_k^2}{\pi} \hbar \omega. \quad (4)$$

In the classical case, this SDF describes Markovian dynamics. The correlation functions are then evaluated as¹⁴

$$C^k(t) \simeq \frac{2A_k^2}{\beta_k} \left(1 + \sum_{l=1}^K 2 \right) \delta(t) - \sum_{l=1}^K \frac{2A_k^2 v_l^k}{\beta_k} e^{-v_l^k |t|} \quad (5)$$

and

$$R^k(t) = A_k^2 \delta(t). \quad (6)$$

We consider the case in which the subsystem attaches to only one bath at the same time; thus, the SB coupling strength and temperature of the bath attached to the subsystem are expressed as

$$A(t) = \sum_{k=1}^N A_k \xi_k(t) \quad (7)$$

and

$$T(t) = \sum_{k=1}^N T_k \xi_k(t), \quad (8)$$

respectively. The inverse temperature of the bath is defined as $\beta(t) = 1/k_B T(t)$. The window function (thermostatic field) is defined as

$$\xi_k(t) = \theta(t - t_k) \theta(t_k + \Delta t - t), \quad (9)$$

where $\theta(t)$ is the step function and the time t_k is defined as $t_k = t_0 + (k - 1)\Delta t$, with initial time t_0 and duration Δt .

For N heat baths, the HEOM consist of a $(K \times N)$ -dimensional hierarchy.^{27,28,32} We consider the situation where the difference between the inverse temperatures of successive heat baths, for example, k and $k + 1$, denoted as $\Delta\beta$, and the time duration of each heat bath Δt is expressed as $\hbar\Delta\beta/\Delta t \ll 1$, $\beta(t)$ [or $T(t)$] is considered to change continuously. Under these conditions, the SB coherence among different heat baths [e.g., the k th bath and the $(k + 1)$ th bath] arising from the bathentanglement between different heat baths becomes negligible, while it is still taken into account in the equilibrium and non-equilibrium distributions of the subsystem.³⁸

This allows us to extend the low-temperature quantum Fokker–Planck equations (LT-QFPE)¹⁴ for the set of Wigner distribution functions (WDFs), $W_{\vec{n}}(p, q; t)$, where $\vec{n} = (n_1, \dots, n_K)$ is the nonnegative integer vector that serves as the index of the hierarchy members by introducing time-dependent Matsubara frequencies $\nu(t) = 1/\hbar\beta(t)$.

Thus, the T-QFPE can be expressed as follows:^{33,34}

$$\begin{aligned} \frac{\partial W_{\vec{n}}(p, q; t)}{\partial t} = & - \left(\hat{\mathcal{L}}_{qm}(t) + \sum_{l=1}^K n_l \nu_l(t) + \hat{\Xi}_K(p, q; t) \right) W_{\vec{n}}(p, q; t) \\ & - \sum_{l=1}^K \hat{\Phi}_p(t) W_{\vec{n} + \vec{e}_l}(p, q; t) \\ & - \sum_{l=1}^K n_l \nu_l(t) \hat{\Theta}_l(p, q; t) W_{\vec{n} - \vec{e}_l}(p, q; t), \end{aligned} \quad (10)$$

where \vec{e}_l is the unit vector whose l th element is 1, otherwise 0. The frequency $\nu_l(t)$ is the l th characteristic frequency of the

non-Markovian effect arising from the Matsubara frequency, and K is the number of frequencies.^{6–8} Although the physical meaning is no longer clear, an efficient and simple approach to suppressing K is to use the Padé decomposition represented by $\nu_l(t) = \zeta_l k_B T(t)/\hbar$, where ζ_l is the l th Padé factor for frequency.^{39–41}

In general, the quantum correlations described by the Matsubara frequencies decay quickly and the above equations describe the thermostatic process accurately. However, for a Brownian system, when the correlation time exceeds the time scale of the bath temperature change, the SDF-based description of a thermal bath breaks down. This situation arises when $A(t)$ changes faster than the noise correlation time, breaking the translational symmetry of the reduced equations of motion regarding the position (see Appendix A). In such cases, results must be verified by comparing them with those explicitly including multiple heat baths using the $(K \times N)$ -dimensional hierarchy,³⁸ as has been done for heat transfer processes^{27,28} and for the adiabatic processes of quantum Carnot cycles.³²

The operator $\hat{\mathcal{L}}_{qm}(t)$ is the quantum Liouvillian of the subsystem expressed using the Fourier form of the potential expressed as^{9–13,42–46}

$$\begin{aligned} -\hat{\mathcal{L}}_{qm}(t)W(p, q) \equiv & -\frac{p}{m} \frac{\partial W(p, q)}{\partial q} \\ & -\frac{1}{\hbar} \int_{-\infty}^{\infty} \frac{dp'}{2\pi\hbar} U_W(p - p', q; t) W(p', q), \end{aligned} \quad (11)$$

where

$$U_W(p, q; t) = 2 \int_0^\infty dx \sin\left(\frac{px}{\hbar}\right) \left[U\left(q + \frac{x}{2}; t\right) - U\left(q - \frac{x}{2}; t\right) \right]. \quad (12)$$

While the above representation of Liouvillian is numerically stable even in cases where the potential is singular (the source code for the above scheme is given in the supporting material of Ref. 9), when the potential is in a simple analytical form, we employ the Moyal expansion,^{14,46,47}

$$\begin{aligned} -\hat{\mathcal{L}}_{qm}(t)W(p, q) \equiv & -\frac{p}{m} \frac{\partial W(p, q)}{\partial q} + \sum_{n=0}^{\infty} \frac{1}{(2n+1)!} \frac{\partial^{2n+1} U(q; t)}{\partial q^{2n+1}} \\ & \times \left(-\frac{\hbar^2}{4} \frac{\partial^2}{\partial p^2} \right)^n \frac{\partial W(p, q)}{\partial p}. \end{aligned} \quad (13)$$

The other operators in Eq. (10) are defined as follows:^{33,34}

$$\hat{\Phi}_p(t) \equiv -\frac{A(t)}{\beta(t)} \frac{\partial}{\partial p}, \quad (14)$$

$$\hat{\Theta}_0(p, q; t) = \frac{A(t)\beta(t)}{m} \left(p + \frac{m}{\beta(t)} \frac{\partial}{\partial p} \right), \quad (15)$$

$$\hat{\Theta}_l(p, q; t) \equiv 2A(t)\eta_l \frac{\partial}{\partial p}, \quad (16)$$

for $1 \leq l \leq K$, and

$$\hat{\epsilon}_K(p, q; t) \equiv \hat{\Phi}_p(t) \sum_{l=0}^K \hat{\Theta}_l(p, q; t), \quad (17)$$

where η_l is the l th Padé coefficient. Note that while various numerical techniques have been developed to fit the bath correlation function [Eq. (5)],^{48,49} here we chose the Padé spectral decomposition because ζ_l and η_l are independent of the change in bath temperature over time under the thermostatic process. The factors ζ_l and η_l are listed in Ref. 14. In the numerical simulation, we truncate $W_{\hat{n}}(p, q; t)$ satisfying the condition $\sum_{j=1}^K n_j \leq N$, where N is the truncation integer.^{4,7-9}

The classical limit of T-QFPE is the Kramers equation expressed as^{10-13,47,50}

$$\frac{\partial W(p, q; t)}{\partial t} = -\hat{L}_{cl}(t)W(p, q; t) + \frac{A^2}{m} \frac{\partial}{\partial p} \left(p + \frac{m}{\beta(t)} \frac{\partial}{\partial p} \right) W(p, q; t), \quad (18)$$

where $W(p, q)$ is the phase space distribution function and the classical Liouvillian is defined as

$$-\hat{L}_{cl}(t)W(p, q) \equiv -\frac{p}{m} \frac{\partial W(p, q)}{\partial q} + \frac{\partial U(q; t)}{\partial q} \frac{\partial W(p, q)}{\partial p}. \quad (19)$$

The description of the Kramers equation is equivalent to that of the Langevin equation.^{3,10}

Note that the Wigner representation is also convenient for implementing various boundary conditions, most notably periodic,^{11,12,45} open,⁵¹ and inflow-outflow boundary conditions.⁴²⁻⁴⁴

As presented in Refs. 33 and 34, thermodynamic intensive and extensive variables, which are interrelated by time-dependent Legendre transformations, and various thermodynamic potentials can be evaluated from the T-QFPE. For the potential expressed as $U(q; t) = U_0(q) - x(t)q$, where $U_0(q)$ is the time-independent part of the potential, the enthalpy of the subsystem $H_A(t)$ is expressed as

$$H_A(t) = U_A(t) - x(t)X_A(t), \quad (20)$$

where

$$U_A(t) = \text{tr}_A \left\{ \left[\frac{p^2}{2m} + U_0(q) \right] W(p, q; t) \right\} \quad (21)$$

is the internal energy and

$$X_A(t) = \text{tr}_A \{ qW(p, q; t) \}. \quad (22)$$

Here, $W(p, q; t)$ is the zeroth number of the solution of Eq. (10) expressed as $W_0(p, q, t)$ in the quantum case and the solution of the thermodynamic Kramers Eq. (18) in the classical case.

Details of numerical simulations with T-QFPE are presented in Appendix B.

III. NUMERICAL EXAMINATION FOR ISOTHERMAL BROWNIAN OSCILLATOR SYSTEM

Proceeding with a simulation without verifying computational precision is akin to ascending a cliff without the assurance of a rope. Thus, although limited to the case where the subsystem is harmonic, numerically “exact” tests (non-Markovian tests) for reduced

dynamics of a subsystem under non-perturbative and non-Markovian SB interactions have been developed based on exact analytical solutions of the Brownian oscillator.⁹ Here, non-Markovian effects refer to the effects of time correlations in the noise generated by the heat bath. There are two types of non-Markovianity: one that exists in both the classical and quantum cases, described as the cut-off frequency of SDF, and the other that exists only in the quantum case, described by the Matsubara frequency. Since quantum thermodynamic processes are slower than the bath-noise correlation time, we focus here on the latter non-Markovian effects, which arise even from the Ohmic SDF without a cutoff.

The harmonic potential of the subsystem is described as^{1,2}

$$U(\hat{q}) = \frac{1}{2} m \omega_0^2 \hat{q}^2, \quad (23)$$

where m and ω_0 are the mass and frequency of the subsystem, respectively. In the energy eigenstate representation, the above system is described as $\hat{H}_A = \hbar \omega_0 (\hat{a}^\dagger \hat{a}^- + 1/2)$, where \hat{a}^\pm are the creation-annihilation operators of the eigenstates.

Non-Markovian tests (Ref. 9) are based on the solutions for (i) the steady-state distribution to examine the accuracy of the thermodynamic description, (ii) the symmetric autocorrelation function $C(t) \equiv \langle \hat{q}(t)\hat{q} + \hat{q}\hat{q}(t) \rangle / 2$ to examine the description of temperature effects, (iii) the linear response function $R^{(1)}(t) \equiv i \langle [\hat{q}(t), \hat{q}] \rangle / \hbar$ to examine the description of non-perturbative SB coupling effects, and (iv) the nonlinear response function $R_{\text{TTR}}^{(2)}(t_2, t_1) = -\langle [[\hat{q}^2(t_1 + t_2), \hat{q}(t_1)], \hat{q}] \rangle / \hbar^2$ to test the dynamical correlation between the system and the bath. Here, the equilibrium expectation value is defined as $\langle \dots \rangle = \text{tr} \{ \dots \exp(-\beta \hat{H}_{\text{tot}}) / Z_{\text{tot}} \}$, where Z_{tot} is the partition function for the total Hamiltonian \hat{H}_{tot} . Since the effect of (iv) is not important in the Ohmic case, we perform only tests (i)–(iii).

For all our computations, we fixed the oscillator frequency as $\omega_0 = 1.0$. The temperature was set to (a) $T = 1.0$ (high) and (b) $T = 0.1$ (low). For the T-QFPE, we set the truncation number of the hierarchy to $N = 7$ in tests (i) and (ii), and we set $N = 6, 7$, and 8 for the weak ($A = 0.5$), intermediate ($A = 1.0$), and strong ($A = 1.5$) SB coupling cases in test (iii), respectively. We set the number of Padé frequencies in the T-QFPE to $K = 2$ and 4 at high ($T = 1.0$) and low ($T = 0.1$) temperatures, respectively. The mesh size of the WDF was set to $n_q = 64$ and $n_p = 64$. For the T-QFPE, we chose the mesh steps of $dq = 0.3$ and $dp = 0.5$, and $dq = 0.3$ and $dp = 0.3$ for high ($T = 1.0$) and low ($T = 0.1$) temperatures, respectively. For the Kramers equation, we chose the mesh steps $dq = 0.15$ and $dp = 0.2$, and $dq = 0.3$ and $dp = 0.4$ for high ($T = 1.0$) and low ($T = 0.1$) temperatures, respectively.

To illustrate the applicability of the Markovian assumption (or stochastic thermodynamics), we also present the results obtained from the quantum master equation (QME) in the Lindblad form.⁵² Under the factorized initial condition and rotating wave approximation (RWA) that are employed to preserve positivity under non-realistic Markovian assumption,^{3,4} the QME can be expressed as follows:

$$\begin{aligned} \frac{\partial}{\partial t} \hat{\rho}_A(t) = & -\frac{i}{\hbar} [\hat{H}_A(t), \hat{\rho}_A(t)] + \frac{A^2}{2m} \bar{n} (2\hat{a}^+ \hat{\rho}_A(t) \hat{a}^- - \{\hat{a}^- \hat{a}^+, \hat{\rho}_A(t)\}) \\ & + \frac{A^2}{2m} (\bar{n} + 1) (2\hat{a}^- \hat{\rho}_A(t) \hat{a}^+ - \{\hat{a}^+ \hat{a}^-, \hat{\rho}_A(t)\}), \end{aligned} \quad (24)$$

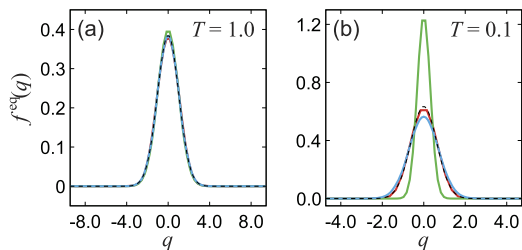


FIG. 1. Non-Markovian tests for the description of (i) the thermal equilibrium state $f^{eq}(q)$ at (a) high temperature ($T = 1.0$) and (b) low temperature ($T = 0.1$) calculated for an Ohmic Brownian oscillator system. In each figure, the calculated results from the T-QFPE (red curve), Kramers equation (green curve), quantum master equation (blue curve), and analytical solution (black dashed curve) are depicted, respectively. The SB coupling strength is $A = 1.0$, and the frequency of the oscillator is $\omega_0 = 1.0$.

where $\bar{n} = 1/(e^{\beta\hbar\omega_0} - 1)$ and we ignored the non-resonant terms, such as $(\hat{a}^+)^2 \hat{\rho}_A(t)$ and $\hat{a}^+ \hat{\rho}_A(t) \hat{a}^+$.³ To perform numerical calculations, we employed 16 eigenstates.

We first examined the descriptions of the thermal equilibrium state as the function of coordinate as¹⁴

$$f^{eq}(q) \equiv \int dp W^{eq}(p, q). \quad (25)$$

In the high-temperature case shown in Fig. 1(a), all calculated results show similar profiles because the thermodynamic characteristic of the subsystem is determined by $\beta\hbar\omega_0$ and the high-temperature limit $\beta \rightarrow 0$ is equivalent to the classical limit $\hbar \rightarrow 0$. However, in the low-temperature case shown in Fig. 1(b), the quantum results are more diffuse than the classical result due to zero-point oscillations. The width of the QME result in Fig. 1(b) is wider than the exact and T-QFPE results due to the lack of bathentanglement.

In Fig. 2, we tested the effects of fluctuations at different temperatures. While the equilibrium distributions were similar, the dynamical behaviors of the T-QFPE and Kramers results were very different from the QME result, especially in the low-frequency regime. This is because RWA ignores the double excitation and de-excitation described by the operators $\hat{a}^+ \hat{a}^+$ and $\hat{a}^- \hat{a}^-$,³ which play

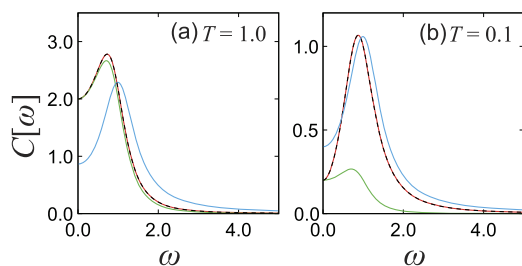


FIG. 2. Non-Markovian test for (ii) the autocorrelation function $C[\omega]$ to examine the effects of temperature effects. In each figure, the results calculated from the T-QFPE (red curve), Kramers equation (green curve), quantum master equation (blue curve), and analytical solution (black dashed curve) are plotted as a function of ω . The SB coupling strength was $A = 1.0$, and the bath temperatures were (a) $T = 1.0$ (high) and (b) $T = 0.1$ (low).

an important role in high-temperature regimes where the thermal excitation energy is large. At low temperatures, the effect of double excitation and de-excitation is suppressed, and the QME and T-QFPE results become closer, while the classical Kramers results become very different due to the lack of zero-point oscillation. The difference between the QME and the T-QFPE results is due to bathentanglement, which becomes apparent at low temperatures.

In Fig. 3, we tested the effects of dissipation at different SB coupling strengths. As the analytical solution of the harmonic Brownian system indicated,¹⁹ the linear response function does not exhibit any quantum effects and the analytical, T-QFPE, and Kramers results always overlap, while the results obtained from the QME differ from

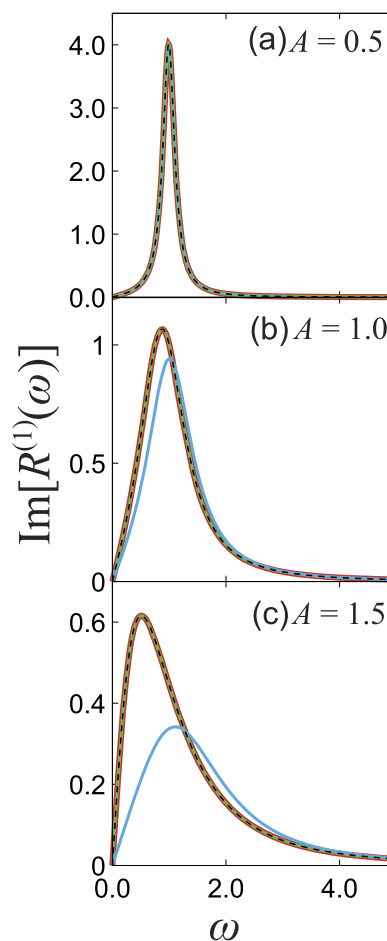


FIG. 3. Non-Markovian test on (iii) the linear response function $\text{Im}[R^{(1)}(\omega)]$ to investigate the description of non-perturbative SB coupling effects. In each figure, the results computed from the T-QFPE (red curve), the Kramers equation (green curve), the quantum master equation (blue curve), and the analytical solution (black dashed curve) are plotted as a function of ω in the high temperature case $T = 1.0$. The SB coupling strengths are (a) $A = 0.5$ (weak), (b) $A = 1.0$ (intermediate), and (c) $A = 1.5$ (strong). In the weak coupling case, all results overlapped and were indistinguishable. In the case of intermediate and strong coupling strengths, the QME results deviated from the exact results, while the T-QFPE and Kramers results always overlapped with the exact results in this harmonic Brownian case where quantum effects do not play a role.

the others, especially for larger A , because the QME is a perturbative approach.

These results indicate that the equations of motion derived using the Markovian or rotating wave (or secular) approximation, such as the Lindblad equation and QME, can only be applied to high-temperature regions where the subsystem exhibits semiclassical dynamics.^{3,4,8,9} Thus, the validity of the fluctuation theorem⁵³⁻⁵⁵ and stochastic thermodynamics⁵⁶⁻⁶¹ based on a factorized initial condition and/or Markovian assumption, especially in the quantum case, should be carefully examined. In addition, as can be seen from the form of Eq. (10), it is the fluctuation and dissipation terms that drive the subsystem to the thermal equilibrium state,⁹ and the detail balance condition is not necessary.³⁴ In fact, the time evolution of the reduced system described by the theory based on the detail balance condition is different from that described by the SB model. Moreover, the HEOM approach, which satisfies the fluctuation–dissipation theorem, can correctly describe the effects of bathentanglement, while theories based on the detailed balance condition ignore them completely.

Before performing a T-QFPE simulation, these tests should be used to select the working parameters, such as mesh size, time step, and hierarchy depth. Since these tests are limited to the case of harmonic potential, a finer choice of mesh and time step is necessary when anharmonicity is large.

IV. DEMONSTRATION WITH THERMOSTATIC STIRLING ENGINE

In conventional studies, the quantum Stirling engine employs two isothermal (hot and cold) processes.⁶²⁻⁶⁵ Here, however, we consider two thermostatic processes, as in the original Stirling engine where the bath temperature changes continuously.³⁴ Thus, the thermostatic Stirling engine consists of four steps: (i) a hot isothermal process, (ii) a thermostatic transition from hot to cold, (iii) a cold isothermal process, and (iv) a thermostatic transition from cold to hot, as described by the external field $E(t)$ and the inverse temperature $\beta(t)$ in Table I. The amplitudes are set as $E_1 = 0.5$ and $E_2 = 0.2$, with the inverse temperatures of the hot and cold baths being $\beta_H = 1.0$ and $\beta_C = 1.5$. For a subsystem, we consider an anharmonic system, the same as described in Refs. 33 and 34. The potential $U(\hat{q}, t)$ is expressed as

$$U(\hat{q}, t) = U_2\hat{q}^2 + U_3\hat{q}^3 + U_4\hat{q}^4 - E(t)\hat{q}, \quad (26)$$

TABLE I. Time evolutions of the external force [$E(t)$] and temperature [$T(t)$] in a four-step thermostatic Stirling engine with equal time intervals τ . The cycle consists of (i) a hot isothermal process, (ii) a thermostatic transition from hot to cold, (iii) a cold isothermal process, and (iv) a thermostatic transition from cold to hot. We set $\Delta E = E_2 - E_1$ and $\Delta\beta = \beta_C - \beta_H$.

	$E(t)$	$\beta(t)$
(i) Hot isothermal	$E_1 + \Delta Et/\tau$	β_H
(ii) Hot to cold	E_2	$\beta_H + \Delta\beta(t/\tau - 1)$
(iii) Cold isothermal	$E_2 - \Delta E(t/\tau - 2)$	β_C
(iv) Cold to hot	E_1	$\beta_C - \Delta\beta(t/\tau - 3)$

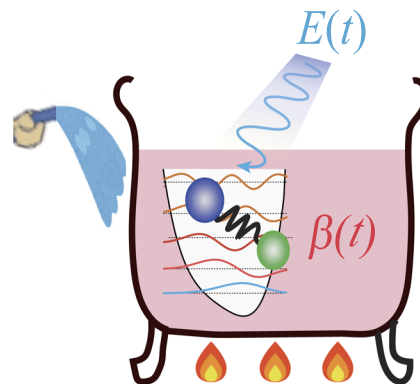


FIG. 4. Schematic illustration of a Stirling engine.

where U_2, U_3 , and U_4 are constants and $E(t)$ is the time-dependent external force. A schematic of the model is presented in Fig. 4. The potential constants are $U_2 = 0.1, U_3 = 0.02$, and $U_4 = 0.05$. We consider (a) weak ($A = 0.5$), (b) intermediate ($A = 1.0$), and (c) strong ($A = 1.5$) SB coupling cases. Additional parameters for the isothermal and thermostatic processes are listed in Table II. The potential surface with the eigenstates and eigenenergies is presented in Ref. 33. In an isothermal process, the first excitation energy is ~ 0.8 , making the bath temperature low at $T = 1/(k_B\beta) \approx 0.3$ and high at $T = 1/(k_B\beta) \approx 5.0$. We present results in the quasi-static case with each step having a time duration of $\tau = 1.0 \times 10^4$, while the non-equilibrium case was discussed in Ref. 34.

In our previous papers,^{33,34} we introduced the quasi-static Massieu potential and dimensionless Clausius entropy defined as

$$\frac{d\Phi_A^{qst}(t)}{dt} = -U_A^{qst}(t) \frac{d\beta^{qst}(t)}{dt} - \tilde{E}^{qst}(t) \frac{dP_A^{qst}(t)}{dt} \quad (27)$$

and

$$\frac{d\Lambda_A^{qst}(t)}{dt} = \beta^{qst}(t) \frac{dU_A^{qst}(t)}{dt} - \tilde{E}^{qst}(t) \frac{dP_A^{qst}(t)}{dt}, \quad (28)$$

respectively, where $\tilde{E}(t) = \beta(t)E(t)$ and the superscript qst indicates that the process is quasi-static. The dimensionless Clausius entropy is related to the quasi-static entropy by $S_A^{qst}(t) = k_B\Lambda_A^{qst}(t)$, allowing us to evaluate the quasi-static entropy using Eq. (28).

TABLE II. Parameter values used for the simulations of the Stirling engine. Here, dx and dp are the mesh sizes for position and momentum, respectively, in the Wigner space. The integers N and K are the cutoff numbers used in the T-QFPE.

	A	N	K	dx	Dp
Classical	0.5	0.25	0.25
	1.0	0.25	0.25
	1.5	0.25	0.25
Quantum	0.5	6	2	0.3	0.5
	1.0	7	2	0.3	0.5
	1.5	8	2	0.3	0.5

To monitor the performance of the thermostatic Stirling engine, we introduced intensive work and heat^{33,34} as follows:

$$\frac{dW_A^{\text{int}}(t)}{dt} = \text{tr}_A \left\{ \frac{\partial \hat{H}_A(t)}{\partial t} \hat{\rho}_A(t) \right\} \quad (29)$$

and

$$\frac{dQ_A(t)}{dt} = \text{tr}_A \left\{ \hat{H}_A(t) \frac{\partial \hat{\rho}_A(t)}{\partial t} \right\}. \quad (30)$$

We provide the demonstration program to evaluate these variables from Eqs. (20) and (21) in the [supplementary material](#).

To elucidate the characteristics of a cyclic process, we constructed thermodynamic work diagrams for external forces, temperature, and their conjugate variables as the $E^{qst}-P_A^{qst}$ and $T^{qst}-S_A^{qst}$ diagrams, analogous to the $P-V$ diagram for a gas system. The work diagrams in the non-equilibrium state are given in Ref. 34. [Figures 5 and 6](#) show the $E^{qst}-P_A^{qst}$ and $T^{qst}-S_A^{qst}$ diagrams for weak and strong SB coupling strengths in the classical (left column) and quantum (right column) cases. The trajectories of the work diagrams are periodic and closed because P_A^{qst} and S_A^{qst} are state variables.

The processes in the $E^{qst}-P_A^{qst}$ diagrams evolve counterclockwise, while those in the $T^{qst}-S_A^{qst}$ diagrams evolve clockwise. Compared to the $P-V$ diagram for an ideal gas, the rotation directions

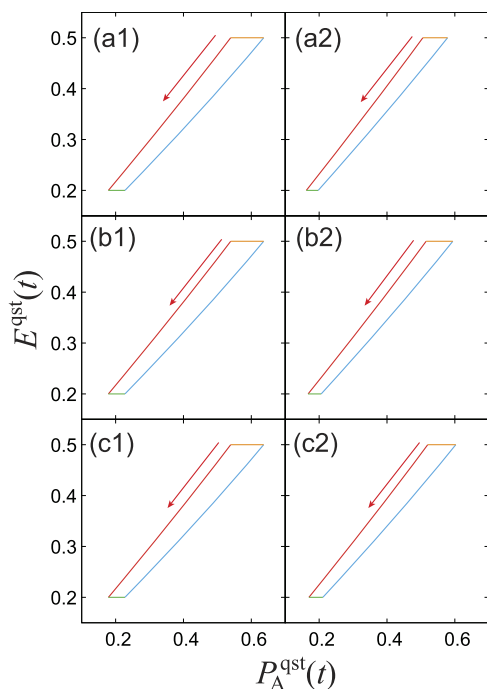


FIG. 5. $E^{qst}(t)-P_A^{qst}(t)$ diagrams for the thermostatic Stirling engine in the classical case (left column) and quantum case (right column) for (a) $A = 0.5$ (weak), (b) 1.0 (intermediate), and (c) 1.5 (strong) SB coupling strengths. In each plot, the four curves (or lines) represent (i) hot isothermal (red), (ii) from hot to cold thermostatic (green), (iii) cold isothermal (blue), and (iv) from cold to hot thermostatic (orange) processes, respectively.

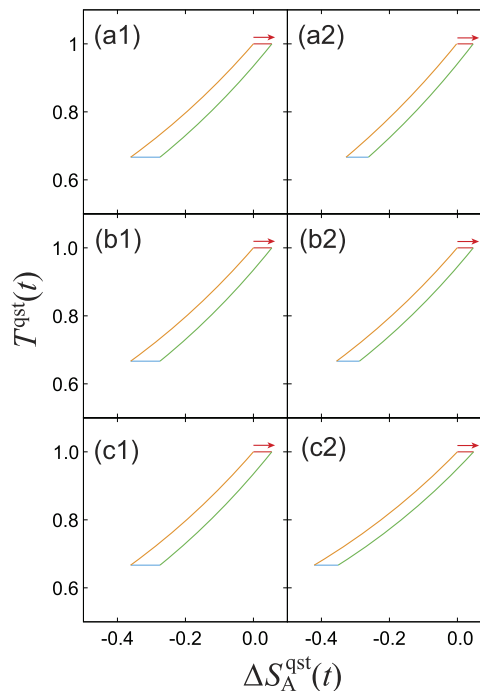


FIG. 6. $T^{qst}(t)-S_A^{qst}(t)$ diagrams for the thermostatic Stirling engine in the classical case (left column) and quantum case (right column) for (a) $A = 0.5$ (weak), (b) 1.0 (intermediate), and (c) 1.5 (strong) SB coupling strengths, respectively. Each cycle starts with the red arrow, and the four curves represent (i) hot isothermal (red), (ii) from hot to cold thermostatic (green), (iii) cold isothermal (blue), and (iv) from cold to hot thermostatic (orange) processes, respectively.

in the $E^{qst}-P_A^{qst}$ diagrams are opposite because the signs of PdV and $E^{qst}dP_A^{qst}$ are opposite in the differential forms of the internal energy in ideal gas and dipole systems. The area enclosed by each diagram corresponds to the positive work performed by the external field in clockwise evolution. We summarize the intensive work [Eq. (29)] performed in one cycle for various SB couplings in the classical and quantum cases in [Table III](#). For the $T^{qst}-S_A^{qst}$ diagrams in [Fig. 6](#), the area enclosed by the clockwise curve corresponds to the heat, Q_A per cycle. The entropy changes monotonically in the thermostatic processes due to the concavity of the quasi-static Gibbs energy for T .³³

In the classical case, the equilibrium distribution is independent of the SB coupling strength, as indicated by the Kramers equation. Therefore, the diagram is the same for the coupling strength. In

TABLE III. The intensive work performed in one cycle is shown for weak ($A = 0.5$), intermediate ($A = 1.0$), and strong ($A = 1.5$) SB coupling strengths in both the classical and quantum cases.

A	Classical	Quantum
0.5	-2.264×10^{-2}	-1.657×10^{-2}
1.0	-2.262×10^{-2}	-1.809×10^{-2}
1.5	-2.258×10^{-2}	-1.913×10^{-2}

the quantum case, due to bathentanglement, the trajectories change depending on SB coupling strength,^{31,32} but the difference is not significant because the temperature is not low, making the results closer to the classical case (see also Table II).

Compared to the non-equilibrium case,³⁴ the trajectories in the quasi-static case are stable and do not fluctuate, even when the interaction is weak.

In the quantum case, the work performed by the external field decreases with larger SB coupling strengths due to bathentanglement, while in the classical case, it does not. Our previous study based on the spin-Boson model for the Carnot cycle³² showed that the intensive work performed in one cycle was independent of the SB coupling strength because the initial and final equilibrium states in isothermal processes were the same regardless of the SB coupling strength. Thus, from the Kelvin–Planck statement, the intensive work performed in the isothermal processes was independent of the SB coupling strength. However, in the present case, because the initial and final equilibrium states in isothermal processes differ depending on the SB coupling strength due to bathentanglement, as shown in Appendix C, the intensive work changes depending on the coupling strength.

Finally, in the classical and high-temperature limits, the T-QFPE results are equivalent to those obtained from the Langevin approach, where a Markovian description is applicable. However, at low temperatures, due to the bathentanglement, the subsystem follows non-factorial and non-Markovian dynamics, and its equilibrium state deviates from the Boltzmann distribution. This indicates that dynamics in a fully quantum regime cannot be described by the fluctuation theorem^{53–55} and stochastic thermodynamics.^{56–61} In other words, the difference between the classical and quantum results represents a breakdown of these theory in the fully quantum regime.

V. CONCLUSION

This study presents a flexible and reliable simulation tool (T-QFPE) designed to enable non-experts in open quantum dynamics theory to quantitatively develop non-equilibrium thermodynamic theories. To ensure numerical reliability and facilitate the determination of working variables, such as mesh size and time step, we included a non-Markovian test routine that compares the numerical results with analytical solutions for a harmonic Brownian system.

The central principle of thermodynamics is that thermal phenomena are described as intensive and extensive variables. Consequently, we introduce extensive variables conjugate to intensive variables as time-dependent physical observables.^{33,34} A routine for calculating the Helmholtz energy in the quasi-static case is included. As a demonstration, a thermostatic Stirling engine for an anharmonic Brownian system is simulated and analyzed in both quantum and classical cases. Through work diagrams, it was shown that due to bathentanglement, the work done on the system by the external field is smaller in the quantum case than in the classical case.

Since the thermodynamic Kramers equation used in this study is equivalent to the Langevin equation for thermostatic processes, it is also possible to explore more complex systems using molecular dynamics simulations in classical cases.

Although our current discussion focuses on an anharmonic Brownian system, the code can be extended to study chemical reaction systems,^{10,11,66,67} ratchet systems,¹² resonant tunneling systems,^{42–44} non-adiabatic transition systems,^{14,45,68} and vibrational modes of liquid water,^{69–72} which have been previously studied with the quantum hierarchical Fokker–Planck approach. This extension, for example, would allow for the investigation of the spatiotemporal distribution of entropy production in ratcheting systems.

When focusing solely on quantum properties, simpler systems such as spin–boson systems, are less computationally demanding and easier to analyze. A computer code for the thermodynamic spin–boson system will be presented in a forthcoming paper.³⁸

SUPPLEMENTARY MATERIAL

Numerical integration codes for the T-QFPE and four demo codes (three for non-Markovian tests and one for the thermostatic Stirling engine) are provided in the [supplementary material](#). The manual can be found in the ReadMe.pdf file.

ACKNOWLEDGMENTS

Y.T. was supported by JSPS KAKENHI (Grant No. B21H01884). S.K. was supported by Grant-in-Aid for JSPS Fellows (Grant No. 24KJ1373).

AUTHOR DECLARATIONS

Conflict of Interest

The authors have no conflicts to disclose.

Author Contributions

Shoki Koyanagi: Investigation (equal); Data curation (lead); Software (lead); Writing – original draft (equal). **Yoshitaka Tanimura:** Conceptualization (lead); Investigation (equal); Funding acquisition (lead); Project administration (lead); Writing – review & editing (lead).

DATA AVAILABILITY

The data that support the findings of this study are available from the corresponding authors upon reasonable request.

APPENDIX A: THE ADIABATIC TRANSITION AND THE TRANSLATIONAL SYMMETRY

When considering the adiabatic transition process, where the SB coupling strength $A(t)$ depends on time, an additional term appears, which is expressed as

$$A(t) \frac{dA(t)}{dt} q \frac{\partial}{\partial p} W_{\pi}(p, q; t), \quad (\text{A1})$$

on the right-hand side of Eq. (10). This term violates the translational symmetry of the reduced system because Eq. (A1) is proportional to the position q , and $dA(t)/dt$ is not negligible unless $A(t)$

changes very slowly. This is due to the ambiguity in defining the noise correlation time of a heat bath when $A(t)$ is time-dependent. However, in our current study, $A(t)$ is constant, so this term vanishes.

APPENDIX B: NUMERICAL IMPLEMENTATION OF THE T-QFPE

As with the LT-QFPE,¹⁴ the T-QFPE are simultaneous differential equations expressed in terms of the reduced density matrix elements or WDF. Due to the complex hierarchical structure, especially at low temperatures, the numerical integration of the T-QFPE is computationally intensive in both memory and central processing unit (CPU) efficiency. Efforts have been made to reduce computational costs by improving the algorithmic and numerical techniques.⁴ For example, continuous efforts have been made to construct efficient hierarchy elements.^{48,49,73–75} Here, we use the Padé spectral decompositions^{39–41} instead of the Matsubara frequency decomposition.^{6–9} In our source code, we employed the Padé factors listed in Ref. 14.

Although not used here, if we wish to handle larger systems, such as a system with a conical intersection,⁷⁶ a numerical algorithm based on the optimization of hierarchical basis sets⁷⁷ and a tensor network algorithm to reduce the number of calculations can be employed.^{78,79}

1. Integration routine

We integrate Eq. (10) using the predictor–corrector approach in conjunction with the Adams–Bashforth and Adams–Moulton methods.⁸⁰ In this approach, we first compute an initial guess of the auxiliary WDFs at the next time step $t + \delta t$, as the “predictor” using the fourth-order Adams–Bashforth method expressed as follows:

$$W_{\vec{n}}^{\text{pred}}(t + \delta t) = W_{\vec{n}}(t) + \frac{\delta t}{24} [55K_{\vec{n}}(t) - 59K_{\vec{n}}(t - \delta t) + 37K_{\vec{n}}(t - 2\delta t) - 9K_{\vec{n}}(t - 3\delta t)], \quad (\text{B1})$$

where $K_{\vec{n}}(t) = \hat{\mathcal{L}}_{\vec{n}}(t)W_{\vec{n}}(p, q; t)$ describes the time evolution of each $W_{\vec{n}}(p, q; t)$ using the Liouvillian for the \vec{n} element expressed as $\hat{\mathcal{L}}_{\vec{n}}(t)$. Then, to refine the initial guess, we compute $W_{\vec{n}}(p, q; t + \delta t)$, as the “corrector” using the fourth-order Adams–Moulton method expressed as

$$W_{\vec{n}}(p, q; t + \delta t) = W_{\vec{n}}(p, q; t) + \frac{\delta t}{24} [9K_{\vec{n}}^{\text{pred}}(t + \delta t) + 19K_{\vec{n}}(t) - 5K_{\vec{n}}(t - \delta t) + K_{\vec{n}}(t - 2\delta t)], \quad (\text{B2})$$

where $K_{\vec{n}}^{\text{pred}}(t) = \hat{\mathcal{L}}_{\vec{n}}(t)W_{\vec{n}}^{\text{pred}}(p, q; t)$. In the predictor–corrector method, the corrector $W_{\vec{n}}(p, q; t + \delta t)$ is regarded as the auxiliary WDF at time $t + \delta t$.

To adapt the predictor–corrector approach, the initial values $W_{\vec{n}}(t - \delta t)$, $W_{\vec{n}}(t - 2\delta t)$, and $W_{\vec{n}}(t - 3\delta t)$ must be prepared. Thus, we use the fourth-order Runge–Kutta method for the first three steps from $t - 3\delta t$ to evaluate the initial values.

The Kramers equation (18) with Eq. (19) is also integrated accordingly.

2. Open Multi-Processing (OMP) and Compute Unified Device Architecture (CUDA)

Because the T-QFPE [Eq. (10)] and the Kramers equation [Eq. (18)] are linear differential equations, parallelizing the routines enhances computational performance. Here, we use two parallelization technologies: Open Multi-Processing (OMP), which parallelizes the CPU cores,^{81–83} and Compute Unified Device Architecture (CUDA), which performs parallelization for the Graphic Processing Unit (GPU).^{14,84–86}

In the [supplementary material](#), we provide two types of T-QFPE programs: one using only OMP and one using both OMP and CUDA technologies. To use CUDA, remove the comment symbol “//” from the third line “//#define UseCUDA” in the “MAIN.h” file.

APPENDIX C: PARTITION FUNCTION OF ANHARMONIC POTENTIAL

We consider an anharmonic subsystem expressed as

$$U(q) = \frac{1}{2}m\omega_0^2q^2 - Eq + U'(q), \quad (\text{C1})$$

where $U'(q)$ is the anharmonic part of the potential. The partition function of any anharmonic Brownian oscillator system can be evaluated using the imaginary HEOM approaches.⁹ Alternatively, when the anharmonicity is weak, the partition function can also be evaluated using the generating functional approach as^{9,87,88}

$$Z_{\text{anh}}^{eq} = \left[1 - \frac{1}{\hbar} \int_0^{\beta\hbar} d\tau' U' \left(\hbar \frac{\partial}{\partial \bar{J}(\tau')} \right) + \frac{1}{2\hbar^2} \int_0^{\beta\hbar} \int_0^{\beta\hbar} d\tau'' d\tau' U'' \left(\hbar \frac{\partial}{\partial \bar{J}(\tau')} \right) U' \left(\hbar \frac{\partial}{\partial \bar{J}(\tau'')} \right) + \dots \right] Z_0[\bar{J}; \beta\hbar] \Big|_{\bar{J}(\tau)=E}, \quad (\text{C2})$$

where $Z_0[\bar{J}; \beta\hbar]$ is the generating functional of the subsystem defined by the potential

$$U(q, \tau) = \frac{1}{2}m\omega_0^2q^2 - \bar{J}(\tau)q. \quad (\text{C3})$$

Because $U(q, \tau)$ is harmonic, we can obtain the generating functional expressed as⁸⁷

$$Z_0[\bar{J}; \beta\hbar] = \frac{1}{\beta\hbar\omega_0} \prod_{n=1}^{\infty} \frac{v_n^2}{\omega_0^2 + v_n + \zeta_n} \times \exp \left[\frac{1}{2\hbar M} \int_0^{\beta\hbar} d\tau \int_0^{\beta\hbar} d\sigma \bar{J}(\tau) \bar{J}(\sigma) \Lambda(\tau - \sigma) \right], \quad (\text{C4})$$

where

$$\Lambda(\tau) = \frac{1}{\beta\hbar} \sum_{n=-\infty}^{\infty} \frac{e^{iv_n\tau}}{\omega_0^2 + v_n + \zeta_n} \quad (\text{C5})$$

and

$$\zeta_n = \frac{1}{m} \int_0^\infty \frac{J(\omega)}{\hbar\omega} \frac{2\nu_n^2}{\omega^2 + \nu_n^2} d\omega. \quad (C6)$$

As indicated in the above expression, the value of the partition function in the quantum case changes as a function of the SB coupling strength through $J(\omega)$, even in the harmonic case, while in the classical case, it remains unchanged.

To apply the above expression, both the anharmonicity and the external field are assumed to be weak. The anharmonic part of the potential is given by

$$U'(q) = U_3 q^3 + U_4 q^4. \quad (C7)$$

From Eqs. (C2)–(C6), we can evaluate the intensive work done in one cycle of the Stirling engine. The difference between classical and quantum values in the Ohmic case is evaluated as

$$W_{QM}^{\text{int}} - W_{CL}^{\text{int}} = \frac{3\hbar U_3}{m} (\beta_H \Lambda_{\beta_H}(0) - \beta_C \Lambda_{\beta_C}(0)) (\epsilon_2 - \epsilon_1) + \frac{6\hbar U_4}{m} (\beta_H \Lambda_{\beta_H}(0) - \beta_C \Lambda_{\beta_C}(0)) (\epsilon_2^2 - \epsilon_1^2), \quad (C8)$$

where $\Lambda_{\beta_H}(0)$ and $\Lambda_{\beta_C}(0)$ are $\Lambda(0)$ at β_H and β_C and $\epsilon_\alpha = E_\alpha/m\omega_0^2$ ($\alpha = 1, 2$). For $U_3, U_4 > 0$, the right-hand side of Eq. (C8) is positive for $E_1 > E_2$ because $\beta_H \Lambda_{\beta_H}(0) - \beta_C \Lambda_{\beta_C}(0)$ becomes negative. This implies that $W_{QM}^{\text{int}} > W_{CL}^{\text{int}}$. Since Λ becomes small with increasing SB coupling strength A , the quantum result approaches the classical result as $A \rightarrow \infty$.

Although our numerical results presented in Sec. III are not in the perturbative regime, the results in Table III can be qualitatively explained by this argument.

REFERENCES

- ¹H. Grabert, P. Schramm, and G.-L. Ingold, "Quantum Brownian motion: The functional integral approach," *Phys. Rep.* **168**, 115–207 (1988).
- ²U. Weiss, *Quantum Dissipative Systems*, 4th ed. (World Scientific, 2012).
- ³Y. Tanimura, "Stochastic Liouville, Langevin, Fokker–Planck, and master equation approaches to quantum dissipative systems," *J. Phys. Soc. Jpn.* **75**, 082001 (2006).
- ⁴Y. Tanimura, "Numerically 'exact' approach to open quantum dynamics: The hierarchical equations of motion (HEOM)," *J. Chem. Phys.* **153**, 020901 (2020).
- ⁵Y. Tanimura and R. Kubo, "Time evolution of a quantum system in contact with a nearly Gaussian–Markoffian noise bath," *J. Phys. Soc. Jpn.* **58**, 101–114 (1989).
- ⁶Y. Tanimura, "Nonperturbative expansion method for a quantum system coupled to a harmonic-oscillator bath," *Phys. Rev. A* **41**, 6676–6687 (1990).
- ⁷A. Ishizaki and Y. Tanimura, "Quantum dynamics of system strongly coupled to low-temperature colored noise bath: Reduced hierarchy equations approach," *J. Phys. Soc. Jpn.* **74**, 3131–3134 (2005).
- ⁸Y. Tanimura, "Reduced hierarchical equations of motion in real and imaginary time: Correlated initial states and thermodynamic quantities," *J. Chem. Phys.* **141**, 044114 (2014).
- ⁹Y. Tanimura, "Real-time and imaginary-time quantum hierarchical Fokker–Planck equations," *J. Chem. Phys.* **142**, 144110 (2015).
- ¹⁰Y. Tanimura and P. G. Wolynes, "Quantum and classical Fokker–Planck equations for a Gaussian–Markovian noise bath," *Phys. Rev. A* **43**, 4131–4142 (1991).
- ¹¹Y. Tanimura and P. G. Wolynes, "The interplay of tunneling, resonance, and dissipation in quantum barrier crossing: A numerical study," *J. Chem. Phys.* **96**, 8485–8496 (1992).
- ¹²A. Kato and Y. Tanimura, "Quantum suppression of ratchet rectification in a Brownian system driven by a biharmonic force," *J. Phys. Chem. B* **117**, 13132–13144 (2013).
- ¹³A. Sakurai and Y. Tanimura, "Does \hbar play a role in multidimensional spectroscopy? Reduced hierarchy equations of motion approach to molecular vibrations," *J. Phys. Chem. A* **115**, 4009–4022 (2011).
- ¹⁴T. Ikeda and Y. Tanimura, "Low-temperature quantum Fokker–Planck and Smoluchowski equations and their extension to multistate systems," *J. Chem. Theory Comput.* **15**, 2517–2534 (2019).
- ¹⁵L. Song and Q. Shi, "Hierarchical equations of motion method applied to nonequilibrium heat transport in model molecular junctions: Transient heat current and high-order moments of the current operator," *Phys. Rev. B* **95**, 064308 (2017).
- ¹⁶H. Gong, Y. Wang, X. Zheng, R. Xu, and Y. Yan, "Nonequilibrium work distributions in quantum impurity system–bath mixing processes," *J. Chem. Phys.* **157**, 054109 (2022).
- ¹⁷C. L. Latune, G. Pleasance, and F. Petruccione, "Cyclic quantum engines enhanced by strong bath coupling," *Phys. Rev. Appl.* **20**, 024038 (2023).
- ¹⁸V. Boettcher, R. Hartmann, K. Beyer, and W. T. Strunz, "Dynamics of a strongly coupled quantum heat engine—Computing bath observables from the hierarchy of pure states," *J. Chem. Phys.* **160**, 094108 (2024).
- ¹⁹S. Gatto, A. Colla, H.-P. Breuer, and M. Thoss, "Quantum thermodynamics of the spin-boson model using the principle of minimal dissipation," [arXiv:2404.12118](https://arxiv.org/abs/2404.12118) [quant-ph] (2024).
- ²⁰N. Makri, "Numerical path integral techniques for long time dynamics of quantum dissipative systems," *J. Math. Phys.* **36**, 2430–2457 (1995).
- ²¹N. Makri and D. E. Makarov, "Tensor propagator for iterative quantum time evolution of reduced density matrices. I. Theory," *J. Chem. Phys.* **102**, 4600–4610 (1995).
- ²²N. Makri and D. E. Makarov, "Tensor propagator for iterative quantum time evolution of reduced density matrices. II. Numerical methodology," *J. Chem. Phys.* **102**, 4611–4618 (1995).
- ²³M. Thorwart, P. Reimann, and P. Hänggi, "Iterative algorithm versus analytic solutions of the parametrically driven dissipative quantum harmonic oscillator," *Phys. Rev. E* **62**, 5808–5817 (2000).
- ²⁴V. Jadhao and N. Makri, "Iterative Monte Carlo for quantum dynamics," *J. Chem. Phys.* **129**, 161102 (2008).
- ²⁵N. Makri, "Blip decomposition of the path integral: Exponential acceleration of real-time calculations on quantum dissipative systems," *J. Chem. Phys.* **141**, 134117 (2014).
- ²⁶D. Segal, A. J. Millis, and D. R. Reichman, "Numerically exact path-integral simulation of nonequilibrium quantum transport and dissipation," *Phys. Rev. B* **82**, 205323 (2010).
- ²⁷A. Kato and Y. Tanimura, "Quantum heat transport of a two-qubit system: Interplay between system–bath coherence and qubit–qubit coherence," *J. Chem. Phys.* **143**, 064107 (2015).
- ²⁸A. Kato and Y. Tanimura, "Quantum heat current under non-perturbative and non-Markovian conditions: Applications to heat machines," *J. Chem. Phys.* **145**, 224105 (2016).
- ²⁹S. Sakamoto and Y. Tanimura, "Numerically 'exact' simulations of entropy production in the fully quantum regime: Boltzmann entropy vs von Neumann entropy," *J. Chem. Phys.* **153**, 234107 (2020).
- ³⁰S. Sakamoto and Y. Tanimura, "Open quantum dynamics theory for non-equilibrium work: Hierarchical equations of motion approach," *J. Phys. Soc. Jpn.* **90**, 033001 (2021).
- ³¹S. Koyanagi and Y. Tanimura, "The laws of thermodynamics for quantum dissipative systems: A quasi-equilibrium Helmholtz energy approach," *J. Chem. Phys.* **157**, 014104 (2022).
- ³²S. Koyanagi and Y. Tanimura, "Numerically 'exact' simulations of a quantum Carnot cycle: Analysis using thermodynamic work diagrams," *J. Chem. Phys.* **157**, 084110 (2022).
- ³³S. Koyanagi and Y. Tanimura, "Classical and quantum thermodynamics described as a system–bath model: The dimensionless minimum work principle," *J. Chem. Phys.* **160**, 234112 (2024).

- ³⁴S. Koyanagi and Y. Tanimura, "Classical and quantum thermodynamics in non-equilibrium regime: Application to thermostatic Stirling engine," *J. Chem. Phys.* **161**, 114113 (2024).
- ³⁵P. Ullersma, "An exactly solvable model for Brownian motion: I. Derivation of the Langevin equation," *Physica* **32**, 27–55 (1966).
- ³⁶P. Ullersma, "An exactly solvable model for Brownian motion: II. Derivation of the Fokker–Planck equation and the master equation," *Physica* **32**, 56–73 (1966).
- ³⁷A. Caldeira and A. Leggett, "Path integral approach to quantum Brownian motion," *Physica A* **121**, 587–616 (1983).
- ³⁸S. Koyanagi and Y. Tanimura, "Thermodynamic hierarchical equations of motion and their application to Carnot engine," [arXiv:2408.02249](https://arxiv.org/abs/2408.02249) [cond-mat.stat-mech] (2024).
- ³⁹J. Hu, R.-X. Xu, and Y. Yan, "Communication: Padé spectrum decomposition of Fermi function and Bose function," *J. Chem. Phys.* **133**, 101106 (2010).
- ⁴⁰B.-L. Tian, J.-J. Ding, R.-X. Xu, and Y. Yan, "Biexponential theory of Drude dissipation via hierarchical quantum master equation," *J. Chem. Phys.* **133**, 114112 (2010).
- ⁴¹J. Hu, M. Luo, F. Jiang, R.-X. Xu, and Y. Yan, "Padé spectrum decompositions of quantum distribution functions and optimal hierarchical equations of motion construction for quantum open systems," *J. Chem. Phys.* **134**, 244106 (2011).
- ⁴²A. Sakurai and Y. Tanimura, "An approach to quantum transport based on reduced hierarchy equations of motion: Application to a resonant tunneling diode," *J. Phys. Soc. Jpn.* **82**, 033707 (2013).
- ⁴³A. Sakurai and Y. Tanimura, "Self-excited current oscillations in a resonant tunneling diode described by a model based on the Caldeira–Leggett Hamiltonian," *New J. Phys.* **16**, 015002 (2014).
- ⁴⁴F. Grossmann, A. Sakurai, and Y. Tanimura, "Electron pumping under non-Markovian dissipation: The role of the self-consistent field," *J. Phys. Soc. Jpn.* **85**, 034803 (2016).
- ⁴⁵T. Ikeda, A. G. Dijkstra, and Y. Tanimura, "Modeling and analyzing a photo-driven molecular motor system: Ratchet dynamics and non-linear optical spectra," *J. Chem. Phys.* **150**, 114103 (2019).
- ⁴⁶W. R. Frensley, "Boundary conditions for open quantum systems driven far from equilibrium," *Rev. Mod. Phys.* **62**, 745–791 (1990).
- ⁴⁷H. Risken and H. Risken, *Fokker–Planck Equation* (Springer, 1996).
- ⁴⁸Z.-H. Chen, Y. Wang, X. Zheng, R.-X. Xu, and Y. Yan, "Universal time-domain Prony fitting decomposition for optimized hierarchical quantum master equations," *J. Chem. Phys.* **156**, 221102 (2022).
- ⁴⁹M. Xu, Y. Yan, Q. Shi, J. Ankerhold, and J. T. Stockburger, "Taming quantum noise for efficient low temperature simulations of open quantum systems," *Phys. Rev. Lett.* **129**, 230601 (2022).
- ⁵⁰H. Kramers, "Brownian motion in a field of force and the diffusion model of chemical reactions," *Physica* **7**, 284–304 (1940).
- ⁵¹Y. Tanimura and Y. Maruyama, "Gaussian–Markovian quantum Fokker–Planck approach to nonlinear spectroscopy of a displaced Morse potentials system: Dissociation, predissociation, and optical Stark effects," *J. Chem. Phys.* **107**, 1779–1793 (1997).
- ⁵²G. Lindblad, "On the generators of quantum dynamical semigroups," *Commun. Math. Phys.* **48**, 119–130 (1976).
- ⁵³M. Esposito, U. Harbola, and S. Mukamel, "Nonequilibrium fluctuations, fluctuation theorems, and counting statistics in quantum systems," *Rev. Mod. Phys.* **81**, 1665–1702 (2009).
- ⁵⁴M. Campisi, P. Hänggi, and P. Talkner, "Colloquium: Quantum fluctuation relations: Foundations and applications," *Rev. Mod. Phys.* **83**, 771–791 (2011).
- ⁵⁵T. Sagawa, "Second law-like inequalities with quantum relative entropy: An introduction," in *Lectures on Quantum Computing, Thermodynamics and Statistical Physics*, Kinki University Series on Quantum Computing (World Scientific, 2012), pp. 120–190.
- ⁵⁶T. Schmiedl and U. Seifert, "Efficiency at maximum power: An analytically solvable model for stochastic heat engines," *Europhys. Lett.* **81**, 20003 (2007).
- ⁵⁷U. Seifert, "Stochastic thermodynamics, fluctuation theorems and molecular machines," *Rep. Prog. Phys.* **75**, 126001 (2012).
- ⁵⁸M. Esposito and C. V. den Broeck, "Second law and Landauer principle far from equilibrium," *Europhys. Lett.* **95**, 40004 (2011).
- ⁵⁹P. Strasberg, *Quantum Stochastic Thermodynamics: Foundations and Selected Applications* (Oxford University Press, 2022).
- ⁶⁰R. Rao and M. Esposito, "Conservation laws shape dissipation," *New J. Phys.* **20**, 023007 (2018).
- ⁶¹C. Cockrell and I. J. Ford, "Stochastic thermodynamics in a non-Markovian dynamical system," *Phys. Rev. E* **105**, 064124 (2022).
- ⁶²F. Wu, L. Chen, F. Sun, C. Wu, and Y. Zhu, "Performance and optimization criteria for forward and reverse quantum Stirling cycles," *Energy Convers. Manage.* **39**, 733–739 (1998).
- ⁶³S. Hamedani Raja, S. Maniscalco, G. S. Paraoanu, J. P. Pekola, and N. Lo Gullo, "Finite-time quantum Stirling heat engine," *New J. Phys.* **23**, 033034 (2021).
- ⁶⁴X.-L. Huang, X.-Y. Niu, X.-M. Xiu, and X.-X. Yi, "Quantum Stirling heat engine and refrigerator with single and coupled spin systems," *Eur. Phys. J. D* **68**, 32 (2014).
- ⁶⁵S. Xia, M. Lv, Y. Pan, J. Chen, and S. Su, "Performance improvement of a fractional quantum Stirling heat engine," *J. Appl. Phys.* **135**, 034302 (2024).
- ⁶⁶Q. Shi, L. Zhu, and L. Chen, "Quantum rate dynamics for proton transfer reaction in a model system: Effect of the rate promoting vibrational mode," *J. Chem. Phys.* **135**, 044505 (2011).
- ⁶⁷J. Zhang, R. Borrelli, and Y. Tanimura, "Proton tunneling in a two-dimensional potential energy surface with a non-linear system–bath interaction: Thermal suppression of reaction rate," *J. Chem. Phys.* **152**, 214114 (2020).
- ⁶⁸T. Ikeda and Y. Tanimura, "Probing photoisomerization processes by means of multi-dimensional electronic spectroscopy: The multi-state quantum hierarchical Fokker–Planck equation approach," *J. Chem. Phys.* **147**, 014102 (2017).
- ⁶⁹T. Ikeda, H. Ito, and Y. Tanimura, "Analysis of 2D THz-Raman spectroscopy using a non-Markovian Brownian oscillator model with nonlinear system–bath interactions," *J. Chem. Phys.* **142**, 212421 (2015).
- ⁷⁰H. Ito and Y. Tanimura, "Simulating two-dimensional infrared-Raman and Raman spectroscopies for intermolecular and intramolecular modes of liquid water," *J. Chem. Phys.* **144**, 074201 (2016).
- ⁷¹H. Takahashi and Y. Tanimura, "Discretized hierarchical equations of motion in mixed Liouville–Wigner space for two-dimensional vibrational spectroscopies of liquid water," *J. Chem. Phys.* **158**, 044115 (2023).
- ⁷²H. Takahashi and Y. Tanimura, "Simulating two-dimensional correlation spectroscopies with third-order infrared and fifth-order infrared-Raman processes of liquid water," *J. Chem. Phys.* **158**, 124108 (2023).
- ⁷³T. Ikeda and G. D. Scholes, "Generalization of the hierarchical equations of motion theory for efficient calculations with arbitrary correlation functions," *J. Chem. Phys.* **152**, 204101 (2020).
- ⁷⁴H. Takahashi, S. Rudge, C. Kaspar, M. Thoss, and R. Borrelli, "High accuracy exponential decomposition of bath correlation functions for arbitrary and structured spectral densities: Emerging methodologies and new approaches," *J. Chem. Phys.* **160**, 204105 (2024).
- ⁷⁵B. Le Dé, A. Jaouadi, E. Mangaud, A. W. Chin, and M. Desouter-Lecomte, "Managing temperature in open quantum systems strongly coupled with structured environments," *J. Chem. Phys.* **160**, 244102 (2024).
- ⁷⁶T. Ikeda and Y. Tanimura, "Phase-space wavepacket dynamics of internal conversion via conical intersection: Multi-state quantum Fokker–Planck equation approach," *Chem. Phys.* **515**, 203–213 (2018).
- ⁷⁷D. Hou, S. Wang, R. Wang, L. Ye, R. Xu, X. Zheng, and Y. Yan, "Improving the efficiency of hierarchical equations of motion approach and application to coherent dynamics in Aharonov–Bohm interferometers," *J. Chem. Phys.* **142**, 104112 (2015).
- ⁷⁸Q. Shi, Y. Xu, Y. Yan, and M. Xu, "Efficient propagation of the hierarchical equations of motion using the matrix product state method," *J. Chem. Phys.* **148**, 174102 (2018).
- ⁷⁹R. Borrelli, "Density matrix dynamics in twin-formulation: An efficient methodology based on tensor-train representation of reduced equations of motion," *J. Chem. Phys.* **150**, 234102 (2019).

- ⁸⁰W. H. Press, W. T. Vetterling, S. A. Teukolsky, and B. P. Flannery, *Numerical Recipes* (Cambridge University Press, 1988).
- ⁸¹J. Strümpfer and K. Schulten, “Open quantum dynamics calculations with the hierarchy equations of motion on parallel computers,” *J. Chem. Theory Comput.* **8**, 2808–2816 (2012).
- ⁸²C. Kreisbeck, T. Kramer, and A. Aspuru-Guzik, “Scalable high-performance algorithm for the simulation of exciton dynamics. Application to the light-harvesting complex II in the presence of resonant vibrational modes,” *J. Chem. Theory Comput.* **10**, 4045–4054 (2014).
- ⁸³T. Kramer, M. Noack, J. R. Reimers, A. Reinefeld, M. Rodríguez, and S. Yin, “Energy flow in the photosystem I supercomplex: Comparison of approximative theories with DM-HEOM,” *Chem. Phys.* **515**, 262–271 (2018); a part of Special Issue: ultrafast Photoinduced Processes in Polyatomic Molecules: Electronic Structure, Dynamics and Spectroscopy (Dedicated to Wolfgang Domcke on the occasion of his 70th birthday).
- ⁸⁴C. Kreisbeck, T. Kramer, M. Rodríguez, and B. Hein, “High-performance solution of hierarchical equations of motion for studying energy transfer in light-harvesting complexes,” *J. Chem. Theory Comput.* **7**, 2166–2174 (2011).
- ⁸⁵B. Hein, C. Kreisbeck, T. Kramer, and M. Rodríguez, “Modelling of oscillations in two-dimensional echo-spectra of the Fenna–Matthews–Olson complex,” *New J. Phys.* **14**, 023018 (2012).
- ⁸⁶M. Tsuchimoto and Y. Tanimura, “Spins dynamics in a dissipative environment: Hierarchical equations of motion approach using a graphics processing unit (GPU),” *J. Chem. Theory Comput.* **11**, 3859–3865 (2015).
- ⁸⁷K. Okumura and Y. Tanimura, “Unified time-path approach to the effect of anharmonicity on the molecular vibrational spectroscopy in solution,” *J. Chem. Phys.* **105**, 7294–7309 (1996).
- ⁸⁸Y. Tanimura and K. Okumura, “First-, third-, and fifth-order resonant spectroscopy of an anharmonic displaced oscillators system in the condensed phase,” *J. Chem. Phys.* **106**, 2078–2095 (1997).